Taylor & Francis
Taylor & Francis Group

Science

Straight impact crater rim segments on Mercury

Işık S. Yazıcı [a,b], H. C. Jupiter Cheng [a,c], Kelsey T. Crane [d] and Christian Klimczak [a]

[a]Center for Planetary Tectonics at UGA, Department of Geology, University of Georgia, Athens, GA, USA; [b]Institute of Planetary Research, German Aerospace Center (DLR), Berlin, Germany; [c]Department of Geological and Environmental Sciences, Appalachian State University, Boone, NC, USA; [d]Planetary Structural Geology and Tectonics Group, Department of Geosciences, Mississippi State University, Mississippi State, MS, USA

ABSTRACT
The formation of straight impact crater rims is widely accepted to be influenced by preexisting lithospheric structure. We investigate the distribution and orientations of straight crater rim segments across Mercury. We devise a mapping workflow aimed at minimizing distortions of length and orientation that arise when working on projected image mosaics on a global scale and produce a global map of the rims of 7,145 impact craters with diameters between 20 and 400 km. We extract straight rim segments that maintain consistent orientations for at least 10 km to assess their frequency and orientation. Our dataset shows that 83% of craters have straight rim segments that show strong east–west orientations at the poles and weak north–south or random orientations at lower latitudes. This emphasizes the importance of lithospheric structure for impact cratering on Mercury. Our map dataset provides valuable insights for future investigations into the tectonic evolution of Mercury.

1. Introduction

1.1. Polygonal impact craters

Impact cratering is arguably the most common geologic process found on Mercury, as its surface is observed to be heavily cratered and because impact craters are found on small and large scales. Impact craters are landforms that initiate when planetary objects, such as meteorites, asteroids, or comets, hit the solid surface of a larger planetary body and develop in stages after the impact event. Processes occurring during these stages operate radially away or toward the impact site, such that impact craters are commonly circular, rimmed depressions. This description generally holds true irrespective of crater size, rock type, or the age of the crater (Melosh, 2011). However, plan-view geometries of craters better described as polygonal shapes, such as squares, hexagons and even triangles, are commonly observed on planetary surfaces in our Solar System across a wide range of scales (e.g. Aittola et al., 2007, 2010; Beddingfield et al., 2016; Beddingfield & Cartwright, 2020; Eppler et al., 1983; Neidhart et al., 2017; Öhman et al., 2006, 2008, 2010; Weihs et al., 2015; Zeilnhofer & Barlow, 2021) with, perhaps, the most prominent example of a polygonal impact crater being the nearly square Meteor Crater, Arizona (Shoemaker, 1960).

It is widely accepted that the plan-view geometry of impact craters is influenced mainly by (1) obliqueness of impact (e.g. Elbeshausen et al., 2013; Kenkmann et al., 2014), (2) surficial processes of degradation (e.g. Pohn & Offield, 1970), and (3) heterogeneities and strength variations in the target (e.g. Murray & Guest, 1970). The obliqueness of impact has an effect on the ellipticity of the crater shape. While most impacts are likely to be oblique with the highest probabilities of impact angles to follow a distribution centered at 45° (Shoemaker, 1962), the planform crater shape is found to remain circular and not be elliptical for impact angles larger than 10–15° (Bottke et al., 2000; Gault & Wedekind, 1978). Only a handful of elliptical craters that likely resulted from highly oblique impact angles are found on Mercury, such that the effect is not likely to dominate investigations of plan-view crater shapes.

Processes of degradation of the surface affect the morphological appearance and preservation of craters. These processes include scouring of ejecta from nearby impacts, superposition of younger impacts, impact shaking, and ongoing degradation by micrometeorite bombardment and impact gardening. They lead to the gradual erosion of the impact crater by topographic diffusion (e.g. Fassett & Thomson, 2014) or to sudden changes by superposition of other impacts on the original crater. Surficial processes

of degradation act independently of the original crater shape and thus do not substantially alter the underlying bedrock properties. However, the state of degradation of a crater is a measure of the length of time the crater was exposed to the processes causing the degradation, which thus is widely used to categorize craters into crater classes for stratigraphic purposes (Herrick et al., 2018; Kinczyk et al., 2020; Pohn & Offield, 1970; Spudis & Guest, 1988).

Crater classes range from heavily degraded to very fresh. For Mercury, they generally follow three (e.g. Herrick et al., 2018) or five classes (e.g. Kinczyk et al., 2020; Spudis & Guest, 1988). For the categorization into five classes that we will follow in this work and where 1 is most degraded and 5 is freshest, a series of characteristics that are typically considered include the 'crispness' of the rim and its terracing, crater floor-wall boundary, crater floor, ejecta blanket, crater rays, secondary craters, central structures, and the number of superposed craters (Kinczyk et al., 2020).

Heterogeneities and strength variations within the bedrock that pre-date the impacts are generally accepted to directly influence the plan-view shape of the crater rim while the crater is formed (Murray & Guest, 1970; Scott et al., 1977; Shoemaker, 1960). Heterogeneities and strength variations that affect the shape of the final crater include the strength of the target substrate (e.g. Watters et al., 2017), preexisting structures such as faults, folds, and joints (Eppler et al., 1983; Öhman et al., 2008, 2010; Watters et al., 2011), or a combination of both.

In particular, a plan-view polygonal geometry of an impact crater is formed when preexisting structures are utilized during excavation and modification of the cratering process (Eppler et al., 1983). Excavation of bedrock may occur preferentially but also more efficiently along fractures (Eppler et al., 1983; Poelchau et al., 2009; Watters et al., 2011), which causes a strong deviation from the circularity of the crater cavity (Eppler et al., 1983; Öhman et al., 2010). Crater modification leads to formation of the crater rim, which consists of crater rim faults that typically undergo free-surface dip-slip (Spray, 1997). In this process, preexisting joints are likely to be reactivated as crater rim faults, causing portions of the crater rim to follow the structural trends of the underlying structure and, thus, forming polygonal crater shapes (Kenkmann et al., 2013). Meteor Crater in Arizona has been extensively studied for its polygonal shape, as it was emplaced into a target containing three sets of regional joints. Hence, much of the effects of bedrock heterogeneities on crater shapes on other planets are informed by fieldwork there (e.g. Kumar & Kring, 2008; Poelchau et al., 2009).

On other planetary surfaces, the polygonal geometries of impact craters were mapped on photogeologic data and analyzed through various methods. Manual mapping of crater rims and visual selections of straight segments is the primary method in most studies (e.g. Aittola et al., 2007, 2010; Neidhart et al., 2017; Öhman et al., 2005, 2008; Weihs et al., 2015; Zeilhofer & Barlow, 2021). Using this method, polygonal impact craters were commonly defined to be those with at least two intersecting straight rim segments. For craters that have the entire rim preserved, Beddingfield et al. (2016) developed a statistical approach of polygonal impact crater identification, using Pearson's Chi-squared test, to detect uniformity in the distributions of crater rim orientations. If the test rejects a uniform distribution, i.e. a circular crater shape, a crater is classified as being polygonal. Automated techniques have also been used to measure the planview shapes of well-preserved impact craters (Robbins & Riggs, 2023; Tabares-Rodenas et al., 2013; Watters et al., 2017), but their performance becomes less reliable when applied to partially preserved or heavily degraded craters.

On Mercury, polygonal shapes of impact craters have been studied since the first images of the innermost planet were returned by the Mariner 10 spacecraft. Wood et al. (1977) considered most impact craters to be round, but also classified those that are not round as either quasipolygonal, strongly polygonal, or irregular. These authors linked polygonal craters to structure in the subsurface, but no systematic orientations were identified and thus no pervasive fracture system was assumed to be present in Mercury's lithosphere. Dzurisin (1978) mapped and analyzed the orientations of lineaments, including straight impact crater rims. It was found that the structurally controlled shapes of heavily degraded craters pointed to a fracture pattern being established early in Mercury's history, linked to global tectonic processes (e.g. Melosh & Dzurisin, 1978). Informed by MErcury Surface Space ENvironment GEochemistry and Ranging (MESSENGER) fly-by data, Weihs et al. (2015) confirmed that polygonal craters are found globally on Mercury.

1.2. Motivation and goal of this study

Because the plan-view shape of craters is related to structures in the bedrock in which the craters formed, mapping crater rims and extracting their orientations can help us better understand structural trends across the planet. The knowledge gained from straight crater rim orientations can then be applied to investigate otherwise hidden tectonic patterns of a cratered planetary surface (e.g. Beddingfield et al., 2016; Beddingfield & Cartwright, 2020). Mercury is known to possess a heavily cratered surface (Figure 1) that is also tectonically deformed by several global and regional processes; see summary in Byrne et al. (2018). Therefore, it is ideal to study
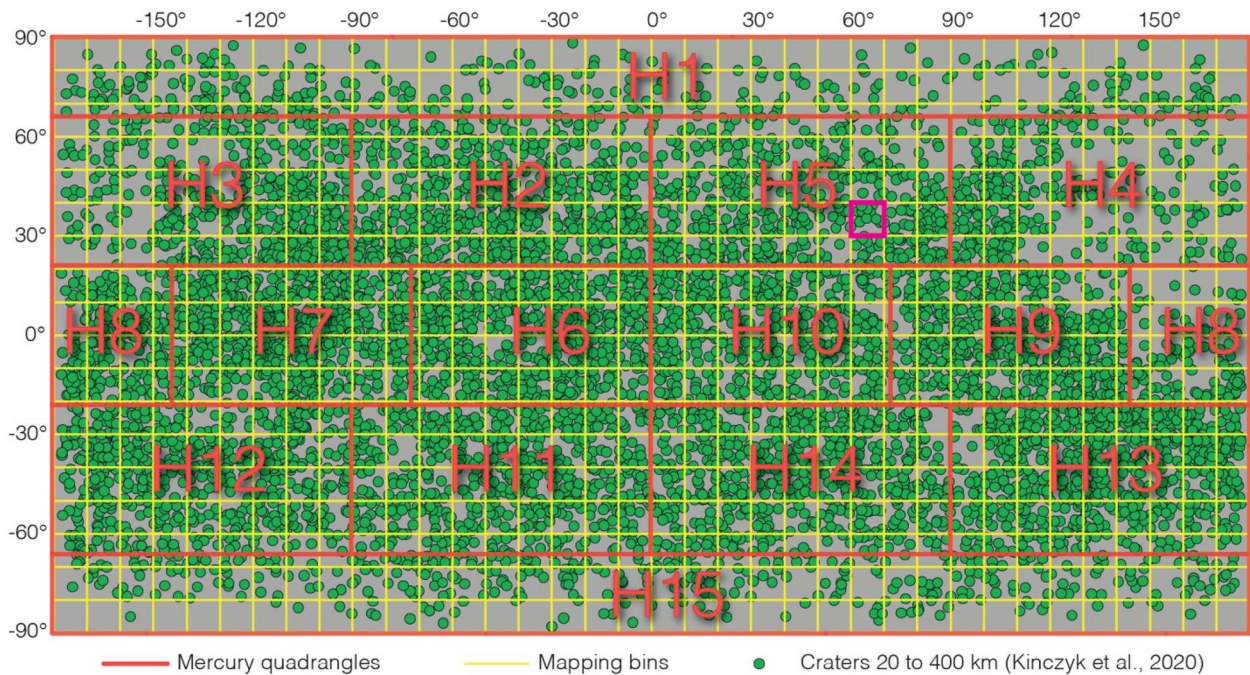
Figure 1. Quadrangle map of Mercury in equirectangular projection showing the centers of impact craters (green dots) from the crater catalog by Kinczyk et al. (2020). Locations of Mercury's quadrangles (outlined in red from H1 to H15) and 10° by 10° bins (yellow lines) that were used for systematic mapping and analysis of crater rim data are shown. Magenta box indicates the location of area in Figure 3.

how plan-view shapes of impact craters that possess various states of degradation reveal hidden structural trends that, in future assessments of our mapping results, can be used to gain insights into the tectonic evolution of Mercury.

The goal of this study is to map the rims of all impact craters with diameters between 20 and 400 km to obtain a comprehensive, internally consistent, and globally representative dataset. This dataset then allows us to quantitatively analyze the distribution and orientation of straight rim segments to visualize structural trends of otherwise hidden sets of fractures across the surface of Mercury. Assignment of degradation classes from the previous analysis (Kinczyk et al., 2020) to our mapped crater rims will aid to place any structural trends into the stratigraphic context of Mercury.

2. Methodology

This research was carried out in three stages. First, impact craters on Mercury were systematically mapped strictly following a mapping algorithm to assure consistency in our data collection across the planet. Second, the mapping facilitated the identification and subsequent extraction of length and orientation data for straight rim segments of craters. Third, the orientations of straight rim segments were visually and statistically analyzed.

The data for this study was collected from MESSENGER image datasets (Denevi et al., 2018) derived

from the Mercury Dual Imaging System (MDIS). The datasets are publicly available from the United States Geologic Survey (USGS) Astropedia lunar and planetary cartographic catalog. In particular, four datasets were used in this research, including the 166 m/pix MESSENGER MDIS monochrome morphology mosaic (Figure 2(a)), two 166 m/pix MESSENGER MDIS high incidence angle mosaics with illumination from east and west (Figure 2(b,c)), and the 665 m/pix digital elevation model (DEM) of Mercury (Becker et al., 2016; Figure 2(d)). A Geographic Information System (GIS) project was created in ESRI's *ArcGIS* software, and the datasets were loaded into the GIS.

We used the existing crater catalogs by Herrick et al. (2018) and Kinczyk et al. (2020) for the identification of the locations of craters. Craters used in this mapping effort include all impact structures between 20 to 400 km in diameter, which includes complex craters to peak-ring basins. The lower cut-off was chosen to limit the number of craters included in this study and to limit uncertainties in crater class categorization, which are more prevalent in smaller craters. The upper cut-off was chosen to avoid inconsistencies of mapping crater rims caused by geometric distortions away from the center of the projection of the map (see below). A total of 7,145 impact craters within the specified diameter range were identified on the surface of Mercury and their center locations were plotted in the GIS as a starting point for the crater rim mapping (Figure 1).
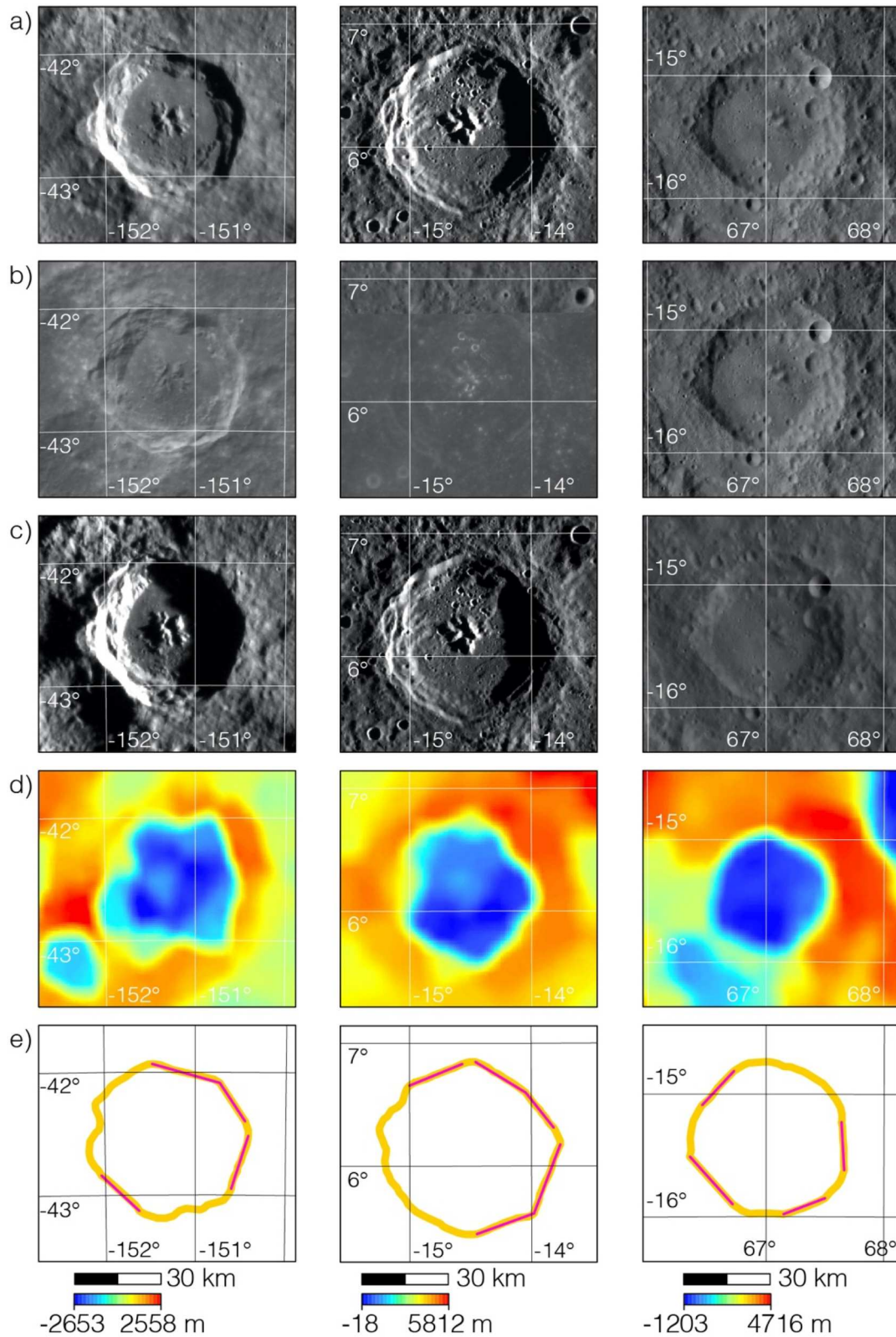
Figure 2. Examples of mapped complex craters with different degradation characteristics. Left column is a fresh impact crater with crisp terraced rim, clear central peak, and no superposed craters. Middle column shows a moderately degraded crater with terraced rim and central peak superposed by several younger impact craters. The right column shows a crater with a heavily degraded crater rim and central peak and many superposed craters. (a) Craters shown on the MESSENGER MDIS monochrome morphology mosaic. (b) The same craters as seen on the MESSENGER MDIS high incidence angle mosaic with illumination from the west. (c) The same craters as seen on the MESSENGER MDIS high incidence angle mosaics with illumination from the east. (d) Craters as they are resolved on the USGS global digital elevation model (DEM) of Mercury. (e) Resultant map of the crater rim displayed in orange and extracted straight crater rim segment shown in red. Note that images may be the same across mosaic datasets and incidence angles may not always be high in the high incidence angle data products due to limitations with image data and mosaicking.

Within the *ArcGIS* ArcCatalog, a geodatabase was created and feature classes were generated for each of the 15 defined Mercury quadrangles, H-1 to H-15 (Figure 1). Line feature classes were chosen as feature class types. The geodatabase was then added to the GIS.

The GIS was set to an azimuthal conformal stereographic projection. Map projected data is prone to distortions. Azimuthal conformal stereographic projections preserve angular relationships through distortions of distances. To minimize length distortions in the mapped line feature class, Mercury's surface was divided into bins of 10° by 10° (Figure 1), and the projection of the map was re-centered onto each bin when mapping within that bin. The projection works well on local scales, and the bin size minimizes length distortions. Mapping was always carried out no more than 5° away from the center of projection. This ensures that distortions of distances between automatically placed vertices spaced equally at 2 km of the line features tracing crater rims (see below) at the edge of the defined bins do not differ from those mapped at the very center by more than ~0.3 km, even for equatorial latitudes, where such bins have the largest areas. The 10° by 10° binning areas do not align perfectly with the quadrangle boundaries. Only craters with center points falling within the quadrangle boundary were mapped for bins straddling two quadrangles.

3. Workflow

3.1. Manual crater mapping

For this research, we performed manual crater rim mapping but also tested a semi-automated crater rim detection method (see supplementary materials S1 and S2). As we find the semi-automated crater rim detection method unsuitable, we will focus on the description of the manual mapping below.

For the purpose of our mapping a crater rim is defined here as the crest or uppermost edge that surrounds the topographic depression caused by the impact. Pristine craters, such as those from crater classes 4 and 5, show a raised rim, a morphological elevation associated with this edge (Kenkmann et al., 2014). The mapping was conducted using the uppermost edge of the crater as observed in the image mosaics, even when more prominent crater terraces were present below the uppermost point. All crater rims but those from highly elliptical craters were mapped. Mapping of all crater rims includes those that are partially preserved because it is possible that some, if not all, straight rim portions may still be preserved and thus may contribute important information to a structural analysis. Including the rims of partially preserved craters minimizes bias towards younger craters, as those are more frequently fully preserved. Mapping only partially preserved crater rims and rim segments instead of full crater rims is not expected to introduce bias in crater rim segment orientation, as cratering is a stochastic process and thus superposition of craters is not expected to preferentially preserve certain crater rim orientations, especially when considering a dataset that includes 7,145 craters. The effect of mapping partially preserved craters on crater rim orientations is also substantially minimized when the data set is processed for extraction of straight rim portions (see below).

Visual inspection of crater rims was carried out on small and large scales using all available datasets (e.g. Figure 2), but the mapping scale for each crater was set as fixed to 1:2,000,000 to ensure consistency of mapping across the entire globe. As stated above, the crater rims were mapped as line feature classes, i.e. polylines, by tracing the crater rims and automatically placing equally spaced vertices at 2 km separation using the stream mode in *ArcMap*. Figure 2(e) shows examples of such mapped crater rims. Discontinuous crater rims were mapped such that multiple rim segments were merged to form one line feature per crater. Each crater rim was assigned a unique identifier to be able to track individual rim segments in any future analyses.

3.2. Data extraction

Next, we determine and isolate straight rim segments. A straight segment is defined as a line feature that maintains an orientation – those portions of crater rims that display no change in orientation or roundedness as one would expect from an ideal crater rim. First, the 'Simplify Line' tool in the *ArcGIS Toolbox* was used to determine and remove the vertices that did not contribute to defining the plan-view crater shape. In particular, the *point remove algorithm* was selected and multiple tolerances, which define the maximum allowable offset of each vertex from its original location, were tested. Among all tolerances tested, the 750 m tolerance worked best to retain the crater shapes but simplify the underlying vertex arrangement. This process allows for identification of sections of crater rims where only two vertices are necessary to describe the orientation and shape of the rim, resulting in straight rim segments.

After simplification, the crater rim polylines were split into individual segments at the remaining vertices using the 'Split Line at Vertices' tool in the *ArcGIS Toolbox*. The spheroidal (geodesic) lengths, coordinates, and orientations of all crater rim segments were computed using the Jenness Enterprises 'Tools for Graphics and Shape' *ArcGIS* plug-in[1] as this method avoids errors caused by map projection distortions that are unaccounted for in the ArcMap

toolbox. By following this mapping procedure, we derive a dataset of straight rim segments from our map. But since longer straight rim segments likely bear higher importance for structural information such as underlying fracture sets, we isolated rim segments longer than 10 km and consider them as straight crater rim segments (Figure 2(e)). We chose the cut-off at 10 km, over twelve times the maximum simplification induced through the 750 m tolerance of the Simplify Line tool, to increase our confidence that no change in orientation occured along those parts of the crater rim.

3.3. Visualization and statistical analysis

Rose diagrams—circular histogram plots that display directional data—were produced to visualize the orientations of the extracted straight rim segments. The calculated lengths of the straight segments were plotted as the counts of the orientations to generate length-weighted rose diagrams. The rose diagrams were all plotted with the scale of 0° to 360° and were displayed to show 36 bins, thus each bin representing 10° of variation in the orientation.

The Kuiper test for uniformity (Kuiper, 1960) was applied to each of our rose diagrams to determine if the length-weighted orientations of the straight rim segments have preferred orientation(s) using the open-access software environment for statistical computing and graphics, *R* (R Core Team, 2019). The Kuiper test of uniformity provides a statistical test to identify preferred orientations by plotting the cumulative frequency, which does not require binning of data, avoiding the visual bias of the rose diagrams. The null hypothesis is that the orientation distribution for crater rims in an area is uniform, i.e. that planform crater shapes are completely circular, and that superposition of impact craters happens randomly. If the Kuiper test returns *p*-values that are less than an alpha level of 0.05, we conclude that there are preferred orientations of crater rims with 95% confidence. If larger *p*-values are returned, rose diagrams may still show preferred orientations, but they are statistically indistinguishable from uniform. The test results are tabulated in section S3 of the supplementary data for our subsequent analysis of global map data.

3.4. Evaluation of workflow

Prior to producing a global map, the robustness of our mapping criteria and efficacy of manual mapping procedure was tested for a 10° by 10° area (Figure 3(a)) by four different mappers. The mapped crater rims are shown in Figure 3(b) and extracted straight rims are shown in Figure 3(c) with color coding corresponding to the four different mappers. Although the mapping styles differed between mappers, for example, by clockwise and counterclockwise mapping of rims
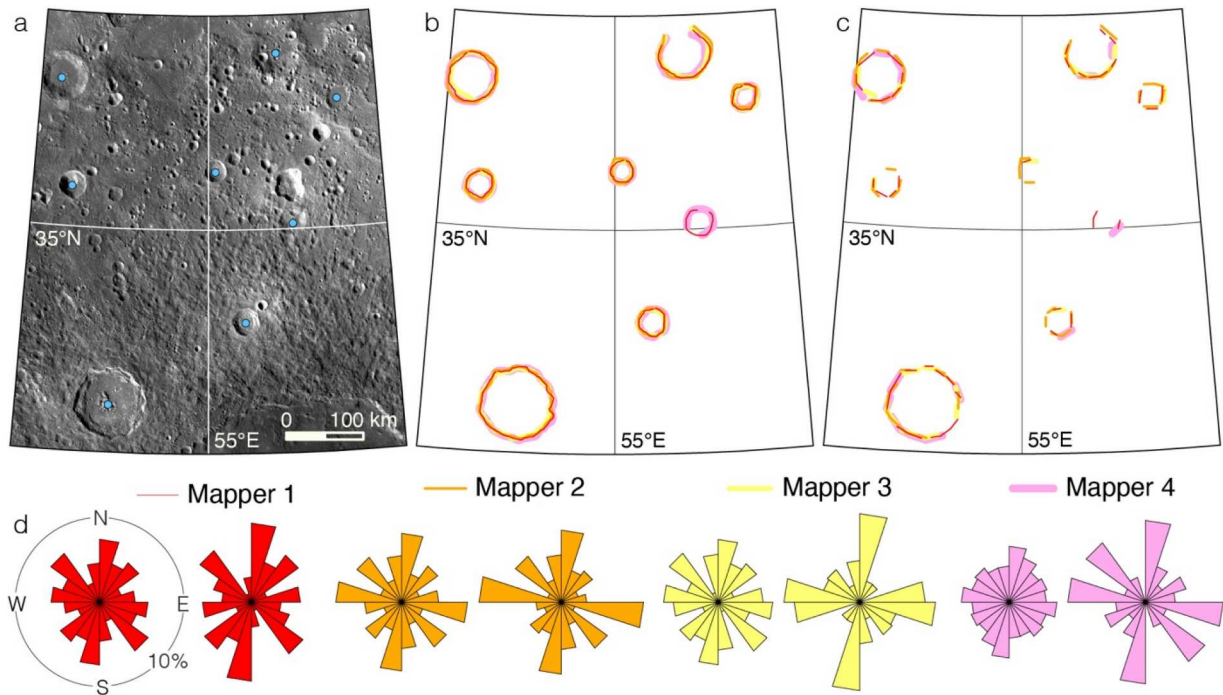

Figure 3. Our 10° by 10° area, centered 35°N, 55°E, used for detailed assessment of our workflow shown in stereographic projection. (a) Eight predefined craters were indicated with blue dots on the imagery. (b) All crater rims were mapped separately by four mappers following the established criteria and procedure. Line features for each mapper are shown in different colors. (c) Straight rim segments were extracted from the line features presented in (b) and are displayed using the same color coding. (d) Length-weighed rose diagrams of each mapper were plotted also using the same color coding for all crater rims (left) and straight rim segments (right).

and by map traces not perfectly overlapping, the overall geometries of crater rims captured are visually similar to one another (Figure 3(b and c)).

For each mapper (Figure 3(d), same color coding), we computed two sets of length-weighed rose diagrams capturing the orientations of all rims and the extracted straight rim segments for all crater within the area (Figure 3(d)). The plots of all crater rims (Figure 3(d), left rose diagram) visually compare well, as their minima and maxima fall in the same bins and display similar distribution of orientations. The plots of straight rim segments (Figure 3(d), right rose diagram) also visually compare well, as their minima and maxima fall in the same bins and display similar distribution of orientations.

We ran a Kolmogorov–Smirnov (K-S) test to compare the distribution of all crater rims to that of the extracted straight rim segments for each mapper. The power of this test is that it accounts for variation within these distributions and looks for similarities in variation between each mapper's work and the group's collective work, testing beyond similarities of means and standard deviations. For example, a crater with north–south and east–west trending straight rim segments would result in a bimodal orientation distribution. While a t-test would not be able to detect the difference between the mapping of this crater or a circular crater with a similar mean orientation, the K-S test would highlight the contrast in variation of the orientation distributions. Thus, when comparing orientation datasets produced by different mappers of the same features, the K-S test is ideal to quantify uniformity in mapping. The K-S test indicates that there is a 54%, 98%, 75%, and 89% chance the distributions of extracted rim segments reflect the distributions of all crater rims for the line features of mappers 1, 2, 3, and 4 respectively. This indicates that the straight rim segment extraction does not significantly change the results, making the workflow robust.

We used a k-sample Anderson–Darling test (Scholz & Stephens, 1987) to compare the empirical distributions of crater rim orientations of each mapper to one another. The Anderson–Darling test is similar to the K-S test in that it emphasizes the importance of variation in determining sample similarity; however, it is more powerful than the K-S test at detecting differences in smaller samples and can be used to compare multiple samples to one another rather than to a group. Our results indicate that there was a 49% chance that the line features of all mappers captured the same crater rims, and the Anderson–Darling test indicates that there is a 99% chance that we mapped and extracted the same straight rim segments. An improved probability is expected, as this test compared extracted straight rim segments rather than the broader distribution of all rim segments. This result further attests to the robustness of manual mapping using our strict workflow and straight rim extraction and its applicability to investigate if preferred orientations exist.

4. Global application

We mapped a total of 7,145 craters with 20–400 km in diameter and assigned their degradation class (Figure 4). Craters larger than 40 km in diameter were matched with the previously assigned crater class from the catalog by Kinczyk et al. (2020) and craters 20–40 km were assigned by this study using the criteria described in Kinczyk et al. (2020). The dataset is provided as geodatabase file in the supplementary materials of this publication for the community to use and improve. The file tabulates all crater rims separated by quadrangle, listing location, length of line features, and the crater class. We extracted straight crater rim segments longer than 10 km and also display them on the map (Figure 4) and tabulate those findings in Table (1). A total of n = 5,927 (or 83%) of the mapped craters have at least one straight rim segment extracted (Table 1). The calculated total spheroidal length of all mapped impact crater rims is 937,402 km, of which straight crater rim segments constitute 413,807 km (~44%; Table 1). Visual inspection of the map for straight rim orientations shows no clear systematic pattern (Figure 4).

In particular, the most degraded craters (class 1) are the biggest impact crater subgroup with 3,043 structures. A total of 76% of them have at least one straight rim segment. Of the 2,795 class 2 craters, 87% have one or more straight rim segments. A total of 89% of the 958 craters in class 3 show at least one straight rim segment. Of the freshest craters, 92% and 93% have one or more straight rim segments in classes 4 and 5, respectively. Moreover, the percentages for the individual crater classes break down such that class 1 craters have ~39%, class 2 craters have ~46%, class 3 craters have ~47%, and crater classes 4 and 5 both have ~50% of their crater rim lengths considered as straight rim segments (Table 1). These percentage breakdowns show that the number of craters with at least one straight rim segment and the length percentage of crater rim returned as straight is highest for the freshest and lowest for the most degraded craters. These overall trends are likely because straight crater rims are better preserved and more easily identified on fresher craters (e.g. Figure 2).

We extracted a total of 28,979 straight crater rim segments longer than 10 km, and their orientations were used to plot length-weighted rose diagrams. To visualize the geographic variations of the segment orientations, we divided Mercury's surface into 72 geographical bins using a 30° by 30° equirectangular grid. Rose diagrams were plotted for each of these
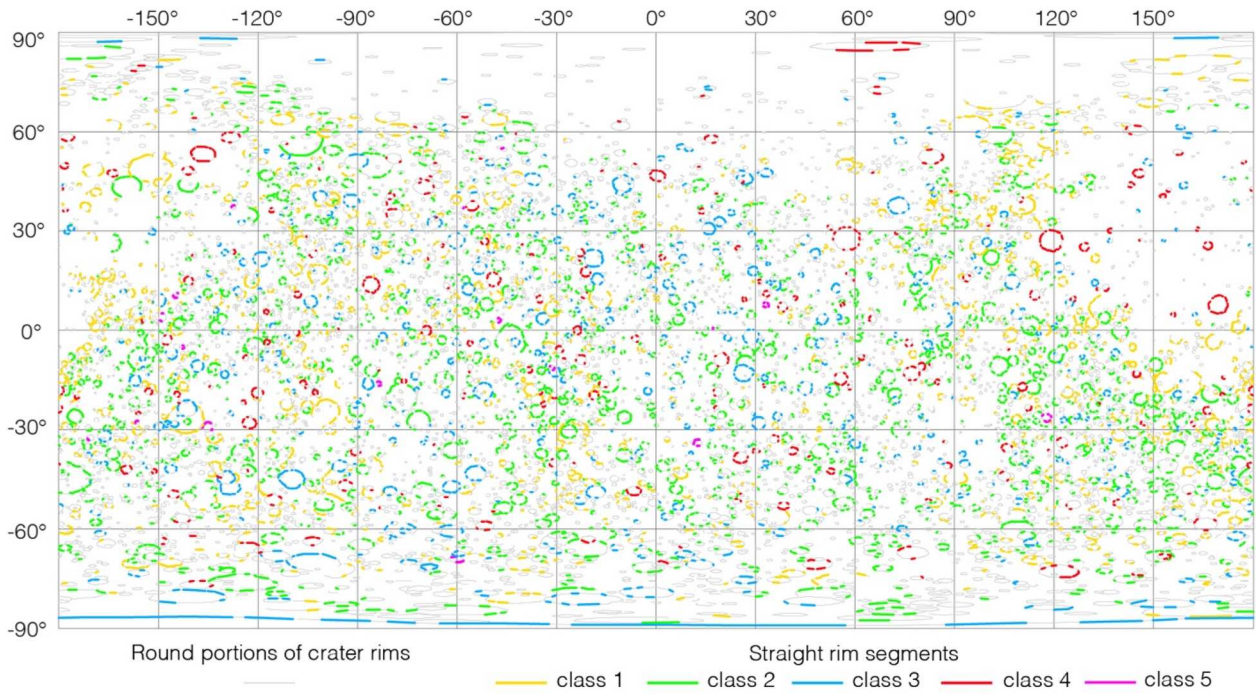
Figure 4. Global map of impact crater rims with diameters between 20 and 400 km on Mercury displayed with gray lines in equirectangular projection. Straight rim segments longer than 10 km are shown to correspond to craters of class 1–5 shown in yellow, green, blue, red, and magenta, respectively. Rims near the poles appear artificially straight due to projection distortions.

Table 1. Table summarizing the analysis of straight crater rims with a breakdown by crater class and total values.

Crater class	Number of craters	Number of straight rim segments	Number of craters with one or more straight rim segments	Length of all mapped crater rims (km)	Length of straight rim segments (km)
Class 1	3,043	8,890	2,316 (76%)	319,843	125,083 (39%)
Class 2	2,795	12,519	2,439 (87%)	386,867	178,743 (46%)
Class 3	958	5,078	849 (89%)	156,784	73,299 (47%)
Class 4	321	2,311	297 (92%)	68,694	34,079 (50%)
Class 5	28	181	26 (93%)	5,214	2,603 (50%)
Total	7,145	28,979	5,927 (83%)	937,402	413,807 (44%)

geographical bins. We also derived the density of measurements by computing the total length of all straight crater rim segments and dividing it by the area of their geographical bin and color coded the rose diagrams accordingly. We tested the data in each of the geographical bins for uniformity using the Kuiper test (see section 3.3.) and shade those geographical bins that have distributions indistinguishable from uniformity in gray.

The map of rose diagrams highlights global and regional variations of straight crater rim orientations across Mercury (Figure 5). All but six geographical bins show rose diagrams with non-uniform distributions of the data, i.e. preferred orientations of straight rim segments, with the six regions also showing preferred orientations but they are statistically indistinguishable from uniform. All polar bins, especially those in the northern hemisphere, show that orientations of straight rim segments have pronounced preferred east–west orientations. We can rule out that this east–west pattern is a function of distortions of mapped distances near the poles, as we

specifically addressed the issue of projection in our mapping criteria. Some equatorial and mid-latitudinal regions show one or more weak preferred orientations of the straight rim segments. One example is a collection of six bins with two preferred north–south and east–west orientations in the northern mid-latitudes between 30°N and 60°N and 90°W and 90°E. Other areas have preferred northeast-southwest and northwest-southeast orientations, especially in the southern mid-latitudes.

As craters and thus their straight rim segments were classified into the different crater classes, additional evaluations are possible to assess whether different subgroups of straight crater rim segments display different orientations (Figure 6). The same analysis to produce and statistically assess rose diagrams was applied to the data for three crater subgroups: for the most heavily degraded craters (classes 1 + 2), moderately degraded craters (class 3) and fresh craters (classes 4 + 5). The density color coding was scaled to be the same for all assessed subgroups to allow for better comparisons of the data.
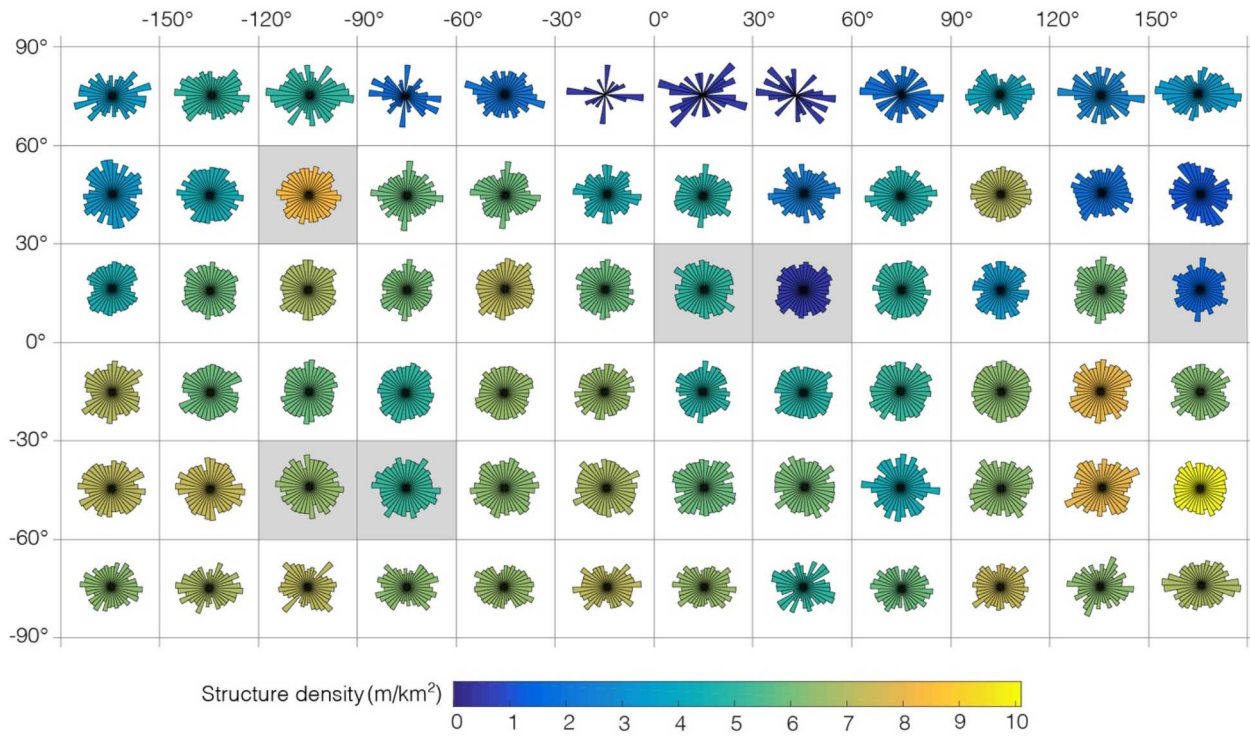
Figure 5. Orientations of straight rim segments on Mercury shown as rose diagrams arranged in equirectangular projection. Density of measurements per bin is color coded with warmer colors representing higher densities and cooler colors representing lower densities. Rose diagrams with orientation distributions indistinguishable from uniform are shown with gray background and those with non-uniform distributions have a white background.

The straight rim segments of heavily degraded impact craters mostly display statistically significant non-uniform orientation distributions with strongly preferred east–west orientations at the poles and various weakly preferred orientations in mid-latitudinal and equatorial regions (Figure 6(a)). The overall pattern and orientations are very similar to the overall the orientations of all crater rim segments (Figure 5), which is expected given that this subgroup includes the majority of the mapped craters and their straight rim segments (Table 1). For moderately degraded craters (Figure 6(b)), a few orientation distributions indistinguishable from uniform are scattered throughout the map but the majority of rose diagrams show preferred orientations of straight crater rim segments. In fact, they show a general trend of east–west preferred orientations at the polar regions but with multiple preferred orientations, ranging from northeast-southwest to northwest-southeast, especially in the south polar region. In the mid-latitudes and equatorial regions, the straight rim segments show multiple preferred orientations but by visual assessment alone, there is no obvious systematic pattern. The sample sizes of straight rim segments of fresh impact craters are smaller, which makes their orientations statistically indistinguishable from uniform in nearly half of the geographical areas (Figure 6(c)). Where preferred orientations are statistically significant, straight crater rim segments show multiple preferred

orientations with no readily visible systematic pattern (Figure 6(c)).

5. Concluding remarks

We produced a map dataset of the rims of all impact craters between diameters of 20 and 400 km on Mercury. The mapping recorded crater rims as line features such that the true shapes of all craters, including those with partially preserved rims and those of different degradation stages, could be recorded. Our mapping workflow was designed to minimize distortions of length and orientation that arise when working on projected image mosaics on a global scale. We used our data to extract straight crater rims of polygonal craters and evaluated for their orientations on a global scale. We find that the majority of craters on Mercury have at least one straight crater rim segment longer than 10 km and that together, these straight rim segments show preferred orientations across the globe and across all crater degradation stages.

We demonstrated that our mapping approach can be applied to a global study that considers all craters and their complexities of preservation. Because incomplete and degraded craters could not be assessed by circular statistics or recognized by semi-automated line detection in previous work, such approaches bias the mapping and analyses toward younger craters that
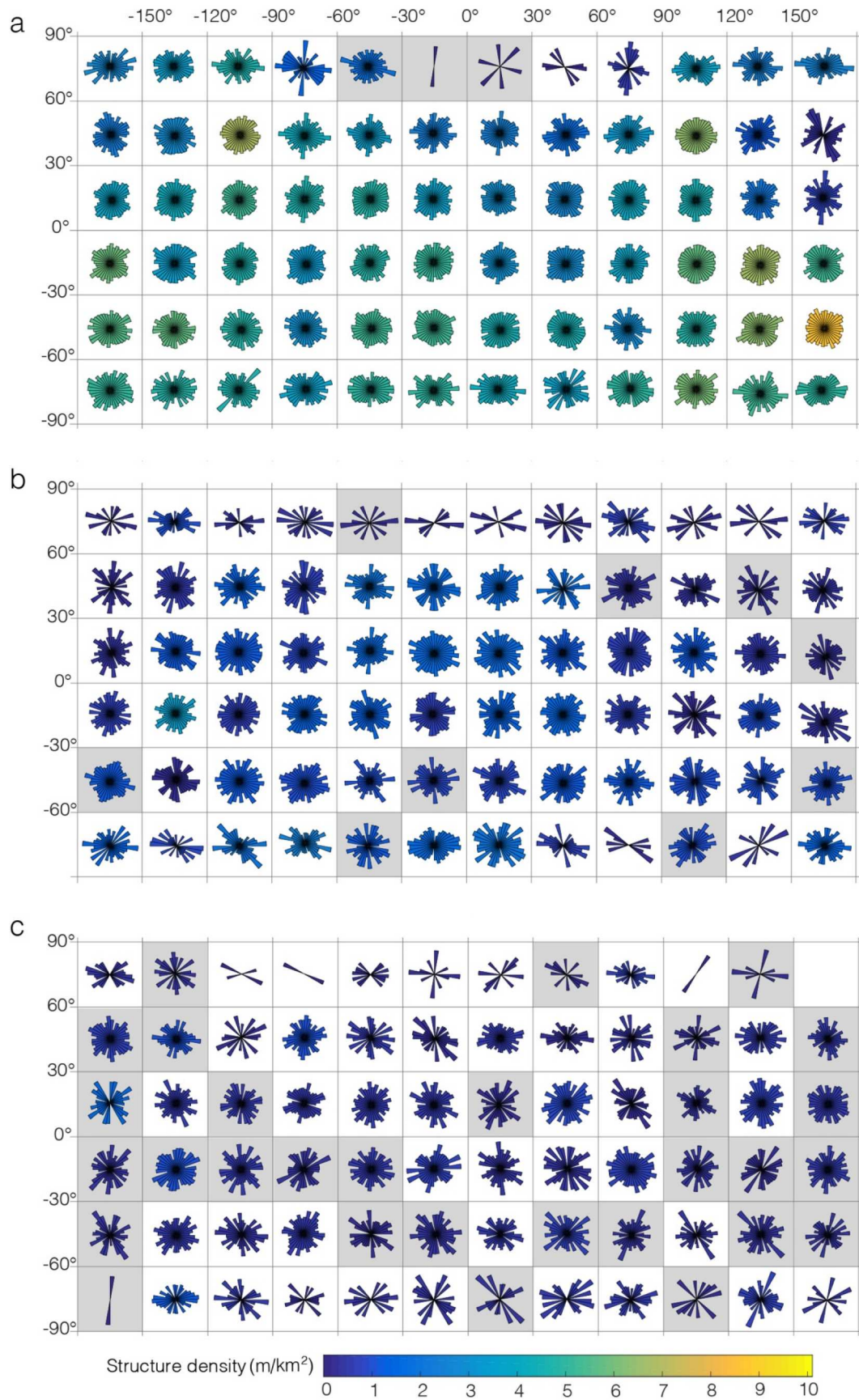
Figure 6. Distribution of straight rim segments on Mercury for subgroups of the different crater classes. (a) Rose diagrams computed from straight rim segments of crater classes 1 and 2. (b) Rose diagrams computed from straight rim segments of class 3 craters. (c) Rose diagrams computed from straight rim segment orientations of crater classes 4 and 5. Color coding of rose diagrams follows the same scheme as in Figure 5.

tend to be best preserved. For analysis of straight crater rim orientations, we also find that grouping craters into geographic regions to increase sample size minimized any possible biases in orientations introduced by the inclusion of partially preserved polygonal craters and allowed us to assess regional trends in orientations.

It is widely accepted that straight rim segments of impact crater rims are related to target heterogeneities, forming parallel to, or directly utilizing pre-existing fractures in the bedrock (e.g. Öhman et al., 2008, 2010; Shoemaker, 1960; Watters et al., 2011). It is therefore likely that the straight crater rim segments that we globally identified across Mercury formed directly along or parallel to a pre-existing tectonic fabric on Mercury, likely consisting of fractures that are otherwise not visible in the available photogeology. Such fractures may include faults that have not produced any noticeable structural relief or sets of joints, similar to those producing the nearly square shape of Meteor crater (Kumar & Kring, 2008; Poelchau et al., 2009; Shoemaker, 1960). Joints, in particular, are the most common types of fractures in rock masses and thus are expected to exist in Mercury's lithosphere. That straight rim segments are found globally and across all crater classes (Figure 4) and that they show preferred orientations (Figures 5 and 6) indicates that Mercury has had a pervasive network of joints with several prominent joint sets throughout most of its geological history. Future structural analysis using this dataset will bring insights into the contribution of joints to the tectonic processes that operated on Mercury.

Software

All mapping was carried out in ArcMap 10.8.2, the rose diagrams were plotted using MATLAB. All statistical analyses were conducted using R. The semi-automated crater rim mapping was conducted using the Unix command-line version of Imagemagick and the masking of crater rims using Inkscape.

Note

1. http://www.jennessent.com/arcgis/shapes_graphics.htm.

Data availability statement

All data used in this mapping effort are freely available. All image mosaics, including the monochrome morphology mosaic and the high incidence angle mosaics with illumination from east and west are available at https://messenger.jhuapl.edu/Explore/Images.html#global-mosaics. Global Mercury digital elevation model is available at https://astrogeology.usgs.gov/search/map/Mercury/Topography/MESSENGER/Mercury_Messenger_USGS_DEM_Global_665m_v2.

ORCID

Işık S. Yazıcı 🆔 http://orcid.org/0000-0002-1172-6566
H. C. Jupiter Cheng 🆔 http://orcid.org/0000-0002-0883-5059
Kelsey T. Crane 🆔 http://orcid.org/0000-0001-5652-053X
Christian Klimczak 🆔 http://orcid.org/0000-0002-6811-8502

References

Aittola, M., Öhman, T., Leitner, J. J., Kostama, V. P., & Raitala, J. (2010). The structural control of Venusian polygonal impact craters. *Icarus*, *205*(2), 356–363. https://doi.org/10.1016/j.icarus.2009.08.004

Aittola, M., Öhman, T., Leitner, J. J., & Raitala, J. (2007). The characteristics of polygonal impact craters on Venus. *Earth, Moon, and Planets*, *101*(1-2), 41–53. https://doi.org/10.1007/s11038-007-9148-4

Becker, K. J., Robinson, M. S., Becker, T. L., Weller, L. A., Edmundson, K. L., Neumann, G. A., Perry, M. E., & Solomon, S. C. (2016). *First global digital elevation model of Mercury*. Lunar and Planetary Science Conference, 47 (Abstract #2959).

Beddingfield, C. B., Burr, D. M., & Tran, L. T. (2016). Polygonal impact craters on Dione: Evidence for tectonic structures outside the wispy terrain. *Icarus*, *274*, 163–194. https://doi.org/10.1016/j.icarus.2016.03.020

Beddingfield, C. B., & Cartwright, R. J. (2020). Hidden tectonism on Miranda's Elsinore Corona revealed by polygonal impact craters. *Icarus*, *343*, Article 113687. https://doi.org/10.1016/j.icarus.2020.113687

Bottke, W. F., Love, S. G., Tytell, D., & Glotch, T. (2000). Interpreting the elliptical crater populations on Mars, Venus, and the Moon. *Icarus*, *145*(1), 108–121. https://doi.org/10.1006/icar.1999.6323

Byrne, P. K., Klimczak, C., & Şengör, A. M. C. (2018). The Tectonic Character of Mercury. In S. Solomon, L. Nittler, & B. Anderson (Eds.), *MERCURY: The View*

after MESSENGER (pp. 249–287). Cambridge University Press.

Denevi, B.W., Chabot, N.L., Murchie, S.L. Becker, K. J., Blewett, D.T., Domingue, D. L., Ernst, C. M., Hash, C. D., Hawkins III, S. D., Keller, M. R., Laslo, N. R., Nair, H., Robinson, M. S., Seelos, F. P., Stephens, G. K., Turner, F.S., & Solomon, S. C. (2018). Calibration, Projection, and Final Image Products of MESSENGER's Mercury Dual Imaging. Space Science Reviews, 214, 2. https://doi.org/10.1007/s11214-017-0440-y

Dzurisin, D. (1978). The tectonic and volcanic history of Mercury as inferred from studies of scarps, ridges, troughs, and other lineaments. *Journal of Geophysical Research: Solid Earth*, 83(B10), 4883–4906. https://doi.org/10.1029/JB083iB10p04883

Elbeshausen, D., Wünnemann, K., & Collins, G. S. (2013). The transition from circular to elliptical impact craters. *Journal of Geophysical Research: Planets*, 118(11), 2295–2309. https://doi.org/10.1002/2013JE004477

Eppler, D. T., Ehrlich, R., Nummedal, D., & Schultz, P. H. (1983). Sources of shape variation in lunar impact craters: Fourier shape analysis. *Geological Society of America Bulletin*, 94(2), 274–291. https://doi.org/10.1130/0016-7606(1983)94<274:SOSVIL>2.0.CO;2

Fassett, C. I., & Thomson, B. J. (2014). Crater degradation on the Lunar Maria: Topographic diffusion and the rate of erosion on the Moon. *Journal of Geophysical Research: Planets*, 119(10), 2255–2271. https://doi.org/10.1002/2014JE004698

Gault, D. E., & Wedekind, J. A. (1978). *Experimental studies of oblique impact*. In Proceedings, 9th Lunar and Planetary Science Conference, pp. 3843–3875.

Herrick, R. R., Bateman, E. M., Crumpacker, W. G., & Bates, D. (2018). Observations from a global database of impact craters on Mercury with diameters greater than 5 km. *Journal of Geophysical Research: Planets*, 123(8), 2089–2109. https://doi.org/10.1029/2017JE005516

Kenkmann, T., Collins, G. S., & Wünnemann, K. (2013). The modification stage of crater formation. In G. R. Osinski, & E. Pierazzo (Eds.), *Impact cratering: Processes and products* (pp. 60–75). Wiley-Blackwell.

Kenkmann, T., Poelchau, M. H., & Wulf, G. (2014). Structural geology of impact craters. *Journal of Structural Geology*, 62, 156–182. https://doi.org/10.1016/j.jsg.2014.01.015

Kinczyk, M. J., Prockter, L. M., Byrne, P. K., Susorney, H. C., & Chapman, C. R. (2020). A morphological evaluation of crater degradation on Mercury: Revisiting crater classification with MESSENGER data. *Icarus*, 341, Article 113637. https://doi.org/10.1016/j.icarus.2020.113637

Kuiper, N. H. (1960). Tests concerning random points on a circle. *Proceedings of the Koninklijke Nederlandse Akademie van Wetenschappen, Series A*, 63(1), 38–47.

Kumar, P. S., & Kring, D. A. (2008). Impact fracturing and structural modification of sedimentary rocks at Meteor Crater, Arizona. *Journal of Geophysical Research: Planets*, 113(E9), E09009. https://doi.org/10.1029/2008JE003115

Melosh, H. J. (2011). Impact cratering. In H. J. Melosh (Ed.), *Planetary surface processes* (pp. 222–275). Cambridge University Press.

Melosh, H. J., & Dzurisin, D. (1978). Mercurian global tectonics: A consequence of tidal despinning? *Icarus*, 35(2), 227–236. https://doi.org/10.1016/0019-1035(78)90007-6

Murray, J. B., & Guest, J. E. (1970). Circularity of craters and related structures on the Earth and Moon. *Modern Geology*, 1, 149–159.

Neidhart, T., Leitner, J., & Firneis, M. (2017). *Polygonal Impact Craters on selected Minor Bodies: Rhea, Dione, Tethys, Ceres, and Vesta*. EGU General Assembly Conference Abstracts (p. 10081).

Öhman, T., Aittola, M., Korteniemi, J., Kostama, V.-P., & Raitala, J. (2010). Polygonal impact craters in the Solar System: Observations and implications. *The Geological Society of America Special Paper*, 465, 51–65.

Öhman, T., Aittola, M., Kostama, V.-P., Hyvärinen, A., & Raitala, J. (2006). Polygonal impact craters in the Argyre region, Mars: Evidence for influence of target structure on the final crater morphology. *Meteoritics & Planetary Science*, 41(8), 1163–1173. https://doi.org/10.1111/j.1945-5100.2006.tb00513.x

Öhman, T., Aittola, M., Kostama, V.-P., & Raitala, J. (2005). The preliminary analysis of polygonal impact craters within greater Hellas region, Mars. *Impact tectonics*, 131–160. https://doi.org/10.1007/3-540-27548-7_5

Öhman, T., Aittola, M., Kostama, V.-P., Raitala, J., & Korteniemi, J. (2008). Polygonal impact craters in Argyre region, Mars: Implications for geology and cratering mechanics. *Meteoritics & Planetary Science*, 43(10), 1605–1628. https://doi.org/10.1111/j.1945-5100.2008.tb00632.x

Poelchau, M. H., Kenkmann, T., & Kring, D. A. (2009). Rim uplift and crater shape in meteor crater: Effects of target heterogeneities and trajectory obliquity. *Journal of Geophysical Research: Planets*, 114, E01006–14. https://doi.org/10.1029/2008JE003235

Pohn, H. A., & Offield, T. W. (1970).). *Lunar crater morphology and relative age determination of lunar geologic units—Part 1. Classification*. US Geological Survey Professional Paper 700-C.

R Core Team. (2019). *R: A language and environment for statistical computing (version 3.5.1) [Computer software]*. R Foundation for Statistical Computing. https://www.R-project.org/

Robbins, S. J., & Riggs, J. D. (2023). What is a polygonal impact crater? A proposed framework toward quantifying crater shapes. *Earth and Space Science*, 10(7), Article e2023EA002863. https://doi.org/10.1029/2023EA002863

Scholz, F. W., & Stephens, M. A. (1987). K-Sample Anderson-Darling tests. *Journal of the American Statistical Association*, 82(399), 918–924. https://doi.org/10.2307/2288805

Scott, D. H., Diaz, J. M., & Watkins, J. A. (1977). *Lunar farside tectonics and volcanism*. Lunar and Planetary Science Conference Proceedings (Vol. 8, 1119–1130).

Shoemaker, E. M. (1960). Penetration mechanics of high velocity meteorites. Illustrated by Meteor Crater, Arizona. 21st International Geological Congress, Copenhagen (pp. 418–434).

Shoemaker, E. M. (1962). Interpretation of lunar craters. In Z. Kopal (Ed.), *Physics and Astronomy of the Moon* (pp. 283–359). Academic Press.

Spray, J. G. (1997). Superfaults. *Geology*, 25(7), 579–582. https://doi.org/10.1130/0091-7613(1997)025<0579:S>2.3.CO;2

Spudis, P. D., & Guest, J. E. (1988). Stratigraphy and geologic history of Mercury. In F. Vilas, C. R. Chapman, & M. S. Matthews (Eds.), *Mercury* (pp. 118–164). University of Arizona Press.

Tabares-Rodenas, P., Ormö, J., & Kring Jr. D. T. (2013). Cosmic wabi-sabi: Tell-tale morphological imperfections in impact crater shapes revealed by numerical analysis. *Earth and Planetary Science Letters*, 377–378, 211–217. https://doi.org/10.1016/j.epsl.2013.06.043

Watters, W. A., Geiger, L. M., Fendrock, M., Gibson, R., & Hundal, C. B. (2017). The role of strength defects in shaping impact crater planforms. *Icarus*, *286*, 15–34. https://doi.org/10.1016/j.icarus.2016.12.024

Watters, W. A., Grotzinger, J. P., Bell III, J., Grant, J., Hayes, A. G., Li, R., Squyres, S. W., & Zuber, M. T. (2011). Origin of the structure and planform of small impact craters in fractured targets: Endurance Crater at Meridiani Planum, Mars. *Icarus*, *211*(1), 472–497. https://doi.org/10.1016/j.icarus.2010.08.030

Weihs, G. T., Leitner, J. J., & Firneis, M. G. (2015). Polygonal impact craters on Mercury. *Planetary and Space Science*, *111*, 77–82. https://doi.org/10.1016/j.pss.2015.03.014

Wood, C. A., Head, J. W., & Cintala, M. J. (1977). Crater degradation on Mercury and the Moon: clues to surface evolution. Proceedings of the 8th Lunar Science Conference. Lunar and Planetary Institute, Houston (pp. 3503–3520).

Zeilnhofer, M. F., & Barlow, N. G. (2021). The characterization and distribution of polygonal impact craters on Ceres and their implications for the cerean crust. *Icarus*, *368*, 114586. https://doi.org/10.1016/j.icarus.2021.114586